Science Advances

AAAS

advances.sciencemag.org/cgi/content/full/2/9/e1601240/DC1

Supplementary Materials for

Quasi-ballistic carbon nanotube array transistors with current density exceeding Si and GaAs

Gerald J. Brady, Austin J. Way, Nathaniel S. Safron, Harold T. Evensen, Padma Gopalan, Michael S. Arnold

Published 2 September 2016, *Sci. Adv.* **2**, e1601240 (2016)
DOI: 10.1126/sciadv.1601240

This PDF file includes:

SUPPLEMENTARY TEXT

Full sweep transfer characteristics:

Example forward and backward sweep $I_{DS} - V_{GS}$ characteristics are plotted in fig. S1, where the forward sweep corresponds to the same data plotted in Fig. 2A. The device exhibits hysteresis, the origin of which has previously been attributed to adsorbed water and oxygen molecules (*64*). Recent work has shown that hysteresis can be eliminated from CNT FETs via encapsulation (*65*).The forward sweep data presented in the main text are more representative of $I_{DS} - V_{GS}$ characteristics in the absence of hysteresis (*66*).

Lead resistance subtraction:

Parasitic lead and wire resistances (R_{leads}) on the order of 100 Ω (accounting for 23% of the total measured resistance (R_{total}) at the highest on-state conductance) are subtracted from R_{total} to obtain the intrinsic device resistance (R_{device}) following

$$R_{device} = R_{total} - R_{leads} \quad (1)$$

To measure R_{leads}, a 30 nm thick, 5 μm wide stripe of Au is deposited and patterned via e-beam lithography, spanning the FET channel from source to drain in order to intentionally electrically short-circuit the FETs. This measurement is performed on each device to account for small pattern-to-pattern differences in lithography and Pd electrode thickness. Example device lead structures and *I-V* measurements for CNT FETs with different lead structure are shown in fig. S2A,B.

Optical spectroscopy evidence of high semiconducting purity:

An absorbance spectrum of the initial dispersion of PFO-BPy sorted arc discharge CNTs in toluene is presented in fig. S3. Metallic CNT peaks, which are typically observed in the range of 630 – 810 nm are not detected (*33*). Previous reports on polyfluorene based sorting of CNTs have estimated the semiconducting CNT purity using the parameter ϕ, which takes into account the area under the CNT absorbance peaks and the absorbance

background (*33, 37*). Ding *et al.* calibrated the ϕ value showing that ϕ = 0.38 corresponds to 99% semiconducting purity (*37*). From our absorbance spectrum in fig. S3 we calculate a higher ϕ of 0.428, which indicates the purity is higher than 99% semiconducting.

Effect of annealing on I_{on}/I_{off}:

To determine whether annealing treatment selectively etches metallic versus semiconducting CNTs, we measure I_{on}/I_{off} and off-conductance (G_{off}) and compare devices without and with 400°C annealing treatment in fig. S4. The I_{on}/I_{off} increases slightly from $10^{4.7\pm1.6}$ to $10^{5.5\pm1.1}$ when comparing devices fabricated without annealing to devices fabricated with 400°C annealing. However, the on-conductance increase caused by annealing the films has a significant contribution to the on/off ratio increase, thus G_{off} is a more direct way to compare the semiconducting purity before and after annealing. G_{off} is $10^{-8.2\pm1.8}$ without annealing and $10^{-8.7\pm1.2}$ with annealing. The similarity in G_{off} with and without annealing suggests the semiconducting purity is not altered significantly by vacuum annealing.

I_{off} variability:

Figure S5A shows that I_{on}/I_{off} exponentially decreases and Fig. 2A shows that ambipolar behavior increases as a function of V_{DS} with a similar trend for three L_{ch} regimes used in this study. Recent work on single CNT FETs demonstrate that ambipolar behavior can be better controlled through design of asymmetric top gate (*67*), dual feedback gate (*60*), or wrap around gate (*61*) architectures to reduce tunneling currents at high V_{DS}. Future implementation of such gate architectures may enable similar electrostatic control over CNT array FETs (*67*). Further analysis of I_{on}/I_{off} is performed at a constant low V_{DS} of -100 mV to shed light on other possible sources of I_{on}/I_{off} variability and L_{ch} trends.

In fig. S5B, I_{on} and I_{off} are presented for 88 "rinsed+annealed" devices as a function of L_{ch},, where I_{on} and I_{off} are the absolute maximum and minimum current, respectively, extracted from the forward sweep of the I_{DS}-V_{GS} transfer curves measured at V_{DS} = -100 mV. I_{off} variability is significant even at low V_{DS}, spanning ~4 orders of

magnitude, and increases at L_{ch} shorter than 250 nm. Several possibilities for the I_{off} variability, leading to I_{on}/I_{off} lower than 10^5 in 30% of devices, are discussed below.

(i) Metallic CNTs are one possible source of I_{off} variability where at shorter channel lengths there is an increased probability that any metallic CNTs that exist in the channel will directly span the source-drain gap. Based on previous *I-V* measurements of single metallic CNTs at positive gate bias we predict a metallic short-circuit would result in a total I_{off} for the CNT arrays (measured at V_{DS} = -100 mV) that is greater than 1 μA (~0.25 μA μm^{-1} for W_{ch} = 4 μm) (*68*). A high I_{off} of 0.3 μA μm^{-1} is observed in only 1 out of 88 devices measured, resulting in a low I_{on}/I_{off} = 300 for this particular device. The remaining 87 devices have I_{off} lower than 0.25 μA μm^{-1} and $I_{on}/I_{off} > 10^3$, suggesting that no metallic CNTs span the channel in these devices.

(ii) CNT-CNT interactions (e.g., due to CNT-crossing or interactions) in the channel may lead to electronic hybridization or dielectric screening effects that increase I_{off} (*15, 17*).

(iii) Another possible factor that may decrease I_{on}/I_{off} and increase the variability of I_{on}/I_{off} is the presence of inhomogeneously distributed fixed and mobile charged impurities at the CNT/SiO_2 interface (*66, 69*). Previous work has indicated that threshold voltage (V_T) variability can be attributed to such inhomogeneity (*70*). In an array FET, if the V_T of each CNT in the array differs then this effect leads to increased subthreshold swing ($SS = (d(\log_{10}(I_{DS})/dV_{GS}))^{-1}$) and decreased I_{on}/I_{off} for the ensemble array (*17*). Cao *et al.* have shown that at short channel lengths surface charge heterogeneity becomes even more prevalent, which further increases V_T variability (*70*). This is consistent with the increased I_{off} variability observed, here, however further studies will be required to decouple the separate contributions of (i), (ii), and (iii) to I_{on}/I_{off} variability and its L_{ch} dependence. In fig. S5C, we plot I_{on}/I_{off} vs. *SS* showing a negative correlation, which could also be attributed to (iii) (*70*). If inhomogeneously distributed fixed and mobile charged impurities or CNT-CNT interactions prove to be the origin of the I_{off} variability in the future then these non-idealities may be improved by implementing high-k dielectrics or by passivating the dielectric surface.

An estimate of the semiconducting CNT purity is obtained from (i), above. We assume that the one device with poor $I_{on}/I_{off} < 10^3$ contains a single metallic CNT. The total number of CNTs that span *S-D* electrodes is 10,208 CNTs (116 per device × 88 devices). From this analysis, we estimate a semiconducting CNT purity greater than 99.99%.

Postdeposition treatment effect on output characteristics:

I_{DS} - V_{DS} curves for "as-deposited" and "rinsed+annealed" samples are plotted for V_{GS} - V_T = -2 V in fig. S6A in order to qualitatively determine the effect of postdeposition treatments on the Pd-CNT injection barrier. Prior to treatment, an injection barrier is present in the "as-deposited" sample, which is evidenced by the highly non-linear I_{DS} - V_{DS} characteristics and increasing differential conductance (dI_{DS}/dV_{DS}) at small V_{DS} > -0.6 V, as shown in fig. S6B. The "rinsed+annealed" treatment significantly reduces this barrier leading to ohmic I_{DS} - V_{DS} characteristics and nearly constant dI_{DS}/dV_D at V_{DS} < -0.3 V.

Protocols used to quantify atomic concentrations from XPS and optical absorbance spectra:

Optical absorbance measurements for CNT and PFO-BPy solutions are presented in fig. S7 where absorbance coefficients are log base 10. CNT concentration (c) is calculated for the S_{22} transition envelope using the relationship

$$\frac{\int_{E_1}^{E_2} A_{S22}^{meas} dE}{c} = \frac{\int_{E_1}^{E_2} A_{S22}^{REF} dE}{c^{REF}} \quad (2)$$

where A_{S22}^{meas} is the measured absorbance of our CNT sample, integrated over the energy range 1.0 –1.8 eV, and A_{S22}^{REF} is the absorbance of a CNT sample of known concentration c^{REF} from Mistry *et al.* (*33*), integrated over the energy range 1.0 –1.8 eV. A PFO-BPy optical cross section ($\sigma_{PFO\text{-}BPy}$) of 1.1 x 10^5 cm^2 g^{-1} was determined by measuring A at 350 nm for a series of dilutions of PFO-BPy reference samples of known concentration. To deconvolute the PFO-BPy absorbance in the CNT@PFO-BPy solution spectrum, we subtract off the contribution of bare CNTs in fig. S7A. The resulting concentrations of CNTs and PFO-BPy are 4.2 and 4.4 μg ml^{-1}, respectively, for the black-line spectrum shown in fig. S7A. Based on this analysis we determine a PFO-BPy:CNT mass ratio of 1.0, and a C:N atomic ratio of 41.

XPS is performed on FESA-deposited films at a packing density of 47 CNTs μm^{-1} (AFM shown in fig. S8). Atomic surface densities (N_i) for i=C, N, and Cl are quantified and summarized in table S1. The N_i are quantified using the SiO_2 substrate as a standard for calibration and the relationship (*71*)

$$N_i = \frac{A_i}{A_{Si}} \frac{S_{Si}}{S_i} \times \left(sin(\theta) \times \lambda_{Si,SiO2} \times \rho_{Si,SiO2}\right) \quad (3)$$

where A_i is the measured peak-area, and A_{Si} is the area of the silicon background peak from the SiO_2 substrate used for calibration. The instrument specific sensitivity factors for each element are S_C =1, S_N = 1.8, S_{Cl} = 2.29, and S_{Si} = 0.82. The measurement take off angle (θ) is 45°, the inelastic mean free path of Si in SiO_2 ($\lambda_{Si,SiO2}$) is 2.96×10^{-7} m, and the density of Si atoms in SiO_2 ($\rho_{Si,SiO2}$) is 2.28×10^{22} atoms cm^{-3}. To check the accuracy of the N_i calculations, we convert the N_C = 1.05×10^{15} C atoms cm^{-2} measured in the "rinsed+annealed" film into a CNT packing density. We subtract off the instrument background C atoms and the C atoms that can be attributed to the PFO-BPy backbone, which can be determined from the known ratio of N to C in the backbone of 1:11. We assume for simplicity that the CNTs are of a single chirality corresponding to the experimental mean diameter of ~1.5 nm (diameter distribution measured in fig. S7B). Based on these assumptions, we estimate a packing density of 57 CNTs μm^{-1}, which is very close to the density of 47 CNT μm^{-1} measured via SEM imaging.

Reduction ratios (*RR*) are reported in the main text and in table S1 to quantify the changes in N_i resulting from post-deposition treatments. These ratios are measured with respect to the "as-deposited" samples.

Control experiments are performed using chloroform ink without CNTs. When these inks are deposited on SiO_2/Si substrates via FESA, the inks do not leave a detectable trace of Cl. These control experiments suggest that the Cl detected in Fig. 3 arises from Cl residues that are directly bonded to the CNTs or PFO-BPy.

<u>Temperature-dependent FTIR measurement of PFO-BPy side chains and backbone</u>:

Thermal degradation of alkyl side chains from PFO-BPy is confirmed by the reduction of the alkyl C-H stretch peaks located at 2855 and 2926 cm^{-1} in Fig. 3C. The spectra are presented as a function of temperature in fig. S9A. The C=C stretching modes are presented, as well, in fig. S9B. In fig. S9A it is evident that the alkyl C-H bonds start to decompose at a temperature in the range of 300 – 400°C. The sp^2 C=C breathing mode is observed at 1450 cm^{-1}, shown in fig. S9B, which originates from the PFO-BPy backbone (*53*). The peak at 1450 cm^{-1} persists after annealing at 400°C, suggesting that the PFO-BPy backbone units remain partially intact following the "rinsed+annealed" post-deposition treatment at 400°C that is used to eliminate the side-chains.

On-conductance comparison of "annealed" versus "rinsed+annealed" treatments:

CNT films having undergone "annealed" and "rinsed+annealed" treatments are compared via electrical measurement in fig. S10 and XPS elemental quantification in table S1. The on-state conductance for FETs constructed from each treatment are similar at each channel length indicating both samples have similar channel and contact resistance. XPS quantities in table S1 show that "annealed" and "rinsed+annealed" samples have similar C, N and Cl reduction ratios. Thus, we conclude annealing is the dominant treatment and that high electronic performance can be achieved with both "annealed" and "rinsed+annealed" treatments.

Conductance per tube measured for FETs with $L_{ch} < 150$ nm:

On-state conductance and the number of CNTs spanning the *S-D* electrodes are measured for 13 CNT array FETs in order to obtain a conductance per tube measurement. These values are plotted in units of quantum conductance ($2e^2/h$) in fig. S11. The SEM images from these short FETs are used to calculate an average packing density of 47 CNTs μm^{-1}.

Contact resistance and mean free path extraction:

A transmission line measurement (*54*) is performed to extract $2R_C$ and L_{MFP} for a set of 88 "rinsed+annealed" CNT array FETs in fig. S12A. There is scatter in the experimentally measured data, and the fit uncertainty in the each of the two parameters is correlated. Thus, to extract possible $2R_C$ and L_{MFP} values, we start by fitting $2R_C$ (*y*-intercept) and the uncertainty in $2R_c$ (σ_{2Rc}) as shown in fig. S12A. Next, we fix $2R_C$ to three values (best fit $2R_C$, best fit $2R_C - \sigma_{2Rc}$, and best fit $2R_C + \sigma_{2Rc}$) and then fit L_{MFP} (which is proportional to the inverse of the slope) for each $2R_C$. The best fit yields $2R_C$ = 34 kΩ-CNT and L_{MFP} = 42 nm. σ_{2Rc} is 6 kΩ-CNT. For $2R_C$ = 28 kΩ-CNT, the fit L_{MFP} = 33 nm. For $2R_C$ = 40 kΩ-CNT, the fit L_{MFP} = 56 nm. These parameters are separately verified using the Y-function method (YFM) (details on YFM extraction method are provided in our previous studies of CNT array FETs (*31*)). We analyze 11 devices with diffusive transport (longer than 225 nm) where $L_{ch} > L_{MFP}$, with results shown in fig. S12B. From YFM analysis we obtain $2R_C$ = 33 – 47 kΩ-CNT, and L_{MFP} = 45 – 63 nm, which agrees well with the ranges obtained from TLM.

Using a simple drift diffusion model, we approximate free carrier mobility for the CNT array

$$\mu = \frac{eL_{MFP}}{v_F m^*} \tag{4}$$

where *e* is the electron charge, v_F is the Fermi velocity in graphene equal to 8×10^5 m s^{-1}, and m^* is the diameter dependent (*d* = 1.5 nm) hole effective mass $m^* = \frac{2\hbar}{3dv_f}$ (*72*). Mobility ranges from 1130 - 1912 cm^2 V^{-1} s^{-1} for the TLM fit L_{MFP} ranging from 33 to 56 nm.

Polymer wrapped CNT diameter distribution:

Optical absorbance spectra of PFO-BPy sorted CNTs in chloroform are measured in order to estimate the diameter distribution from the S_{22} peak in fig. S7B. The S_{22} peak can be fit relatively well to a Gaussian function and from this fit we obtain a diameter distribution of 1.5 ± 0.2 nm based on known chirality-dependent S_{22} energies from literature (*73*).

SUPPLEMENTARY FIGURES AND TABLES

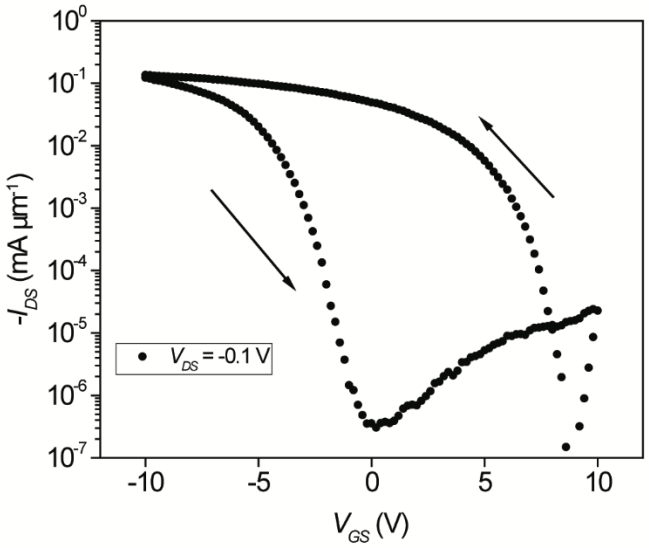

fig. S1. Full sweep transfer characteristics. Full hysteresis loop for CNT array device shown in Fig. 2A. Arrows indicate directions of forward (V_{GS} = -10 → 10 V) and backward (V_{GS} = 10 → -10 V) sweeps.

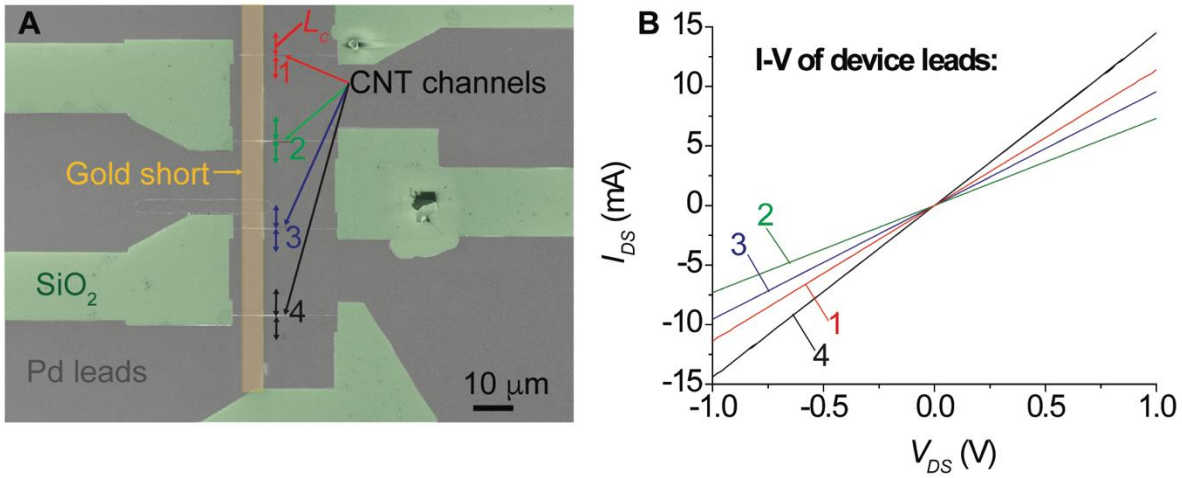

fig. S2. Lead resistance subtraction. (**A**) Top-view false-colored SEM image of CNT array FET lead- and electrode- structure with CNT channel regions and gold stripe short-circuit regions highlighted and labeled. (**B**) *I-V* measurements of leads from different devices, showing some variation in the lead resistance.

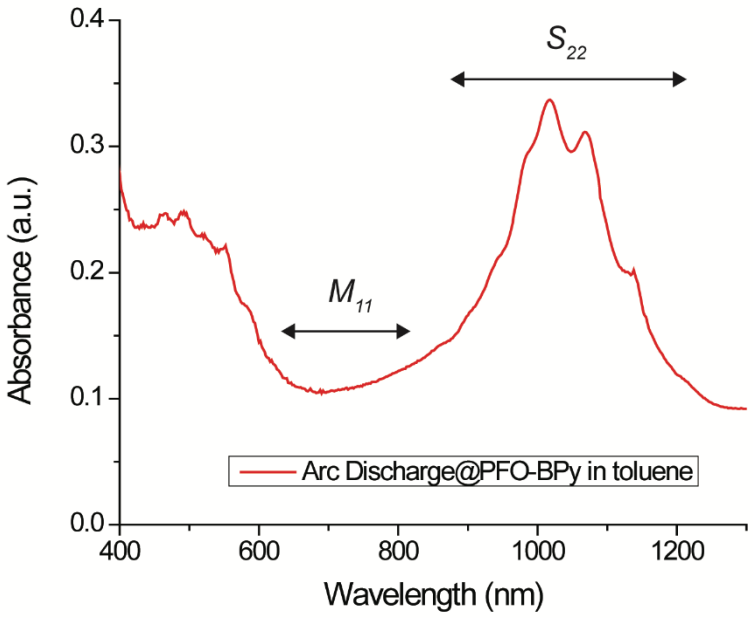

fig. S3. Optical spectroscopy evidence of high semiconducting purity. Absorbance spectrum of PFO-BPy sorted arc discharge CNTs in toluene. No metallic CNTs are detected as evidenced by the absence of a M_{11} peak in the range of 630 – 810 nm. To extract ϕ values, wavelength was converted to energy prior to calculating CNT peak areas.

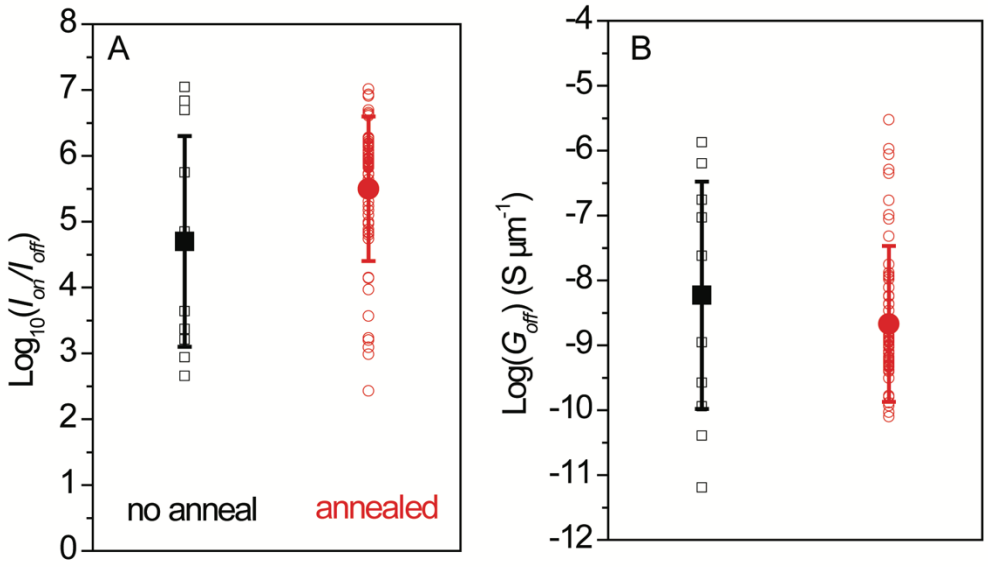

fig. S4. Effect of annealing on I_{on}/I_{off}. Comparison of the on/off ratio (A) and off-conductance (B) of FETs constructed using films without (black squares) versus with (red circles) 400°C annealing treatment. Individual devices are plotted as open symbols, where a total of 10 and 56 devices are measured for without and with annealing treatments, respectively. The mean and standard deviation are also plotted as filled symbols. To ensure a majority of CNTs span the channel, only devices with L_{ch} in the range of 150 – 250 nm are analyzed, with the same mean L_{ch} of ~200 nm for each treatment condition.

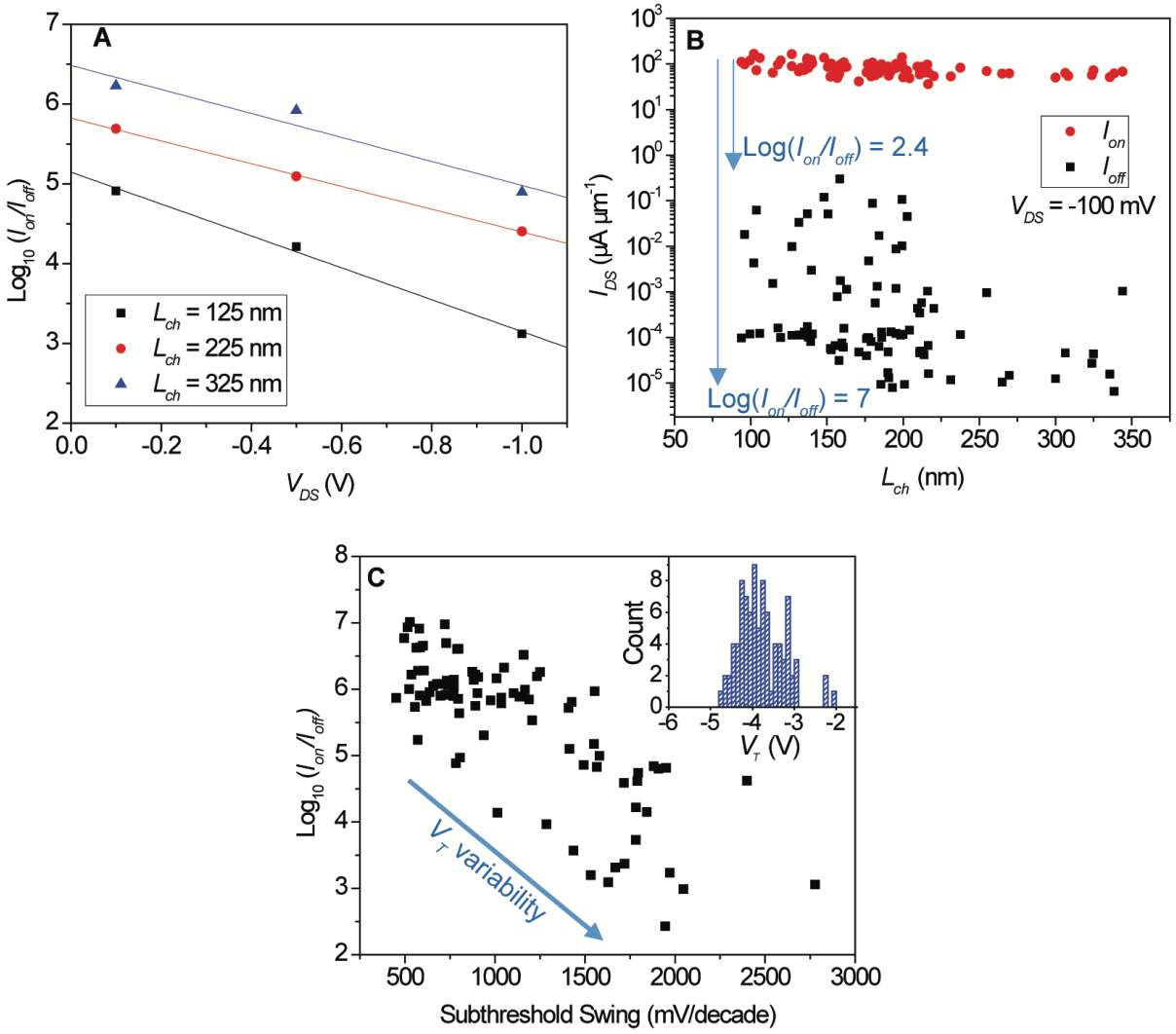

fig. S5. I_{off} variability. (**A**) Exponential decrease in I_{on}/I_{off} as a function of V_{DS} at various L_{ch} regimes. I_{on}/I_{off} is the mean calculated for > 7 devices for L_{ch} ranges of 100-150 nm (125 nm), 200-250 (225 nm), and 300-350 nm (325 nm). (**B**) On and off state current for 88 "rinsed+annealed" devices at various L_{ch}. (**C**) Dependence of I_{on}/I_{off} on sub-threshold swing (*SS*).

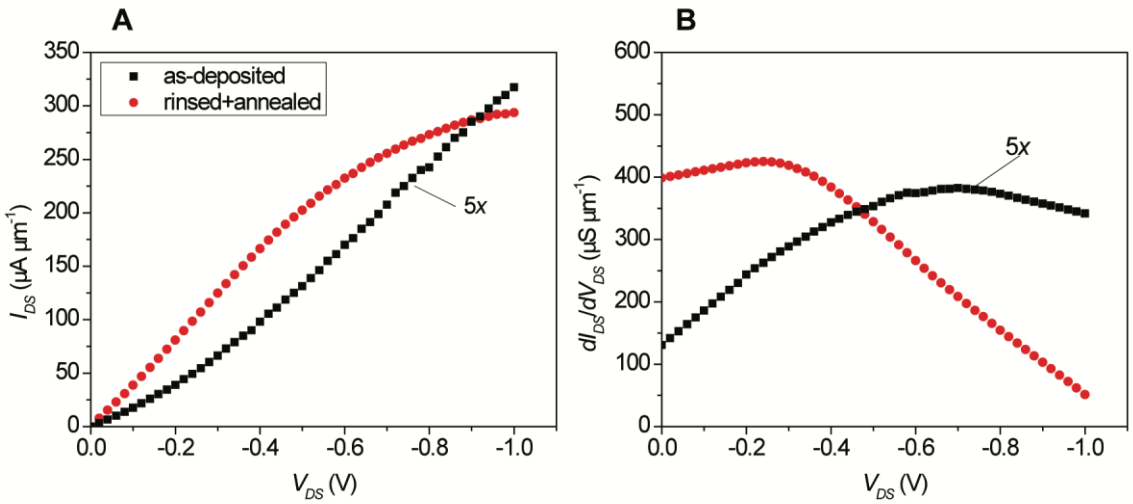

fig. S6. Postdeposition treatment effect on output characteristics. I_{DS} – V_{DS} measurement of "as-deposited" and "rinsed+annealed" CNT array FETs suggest the presence of a Schottky barrier at the Pd-CNT interface of the "as-deposited" CNT array FET.

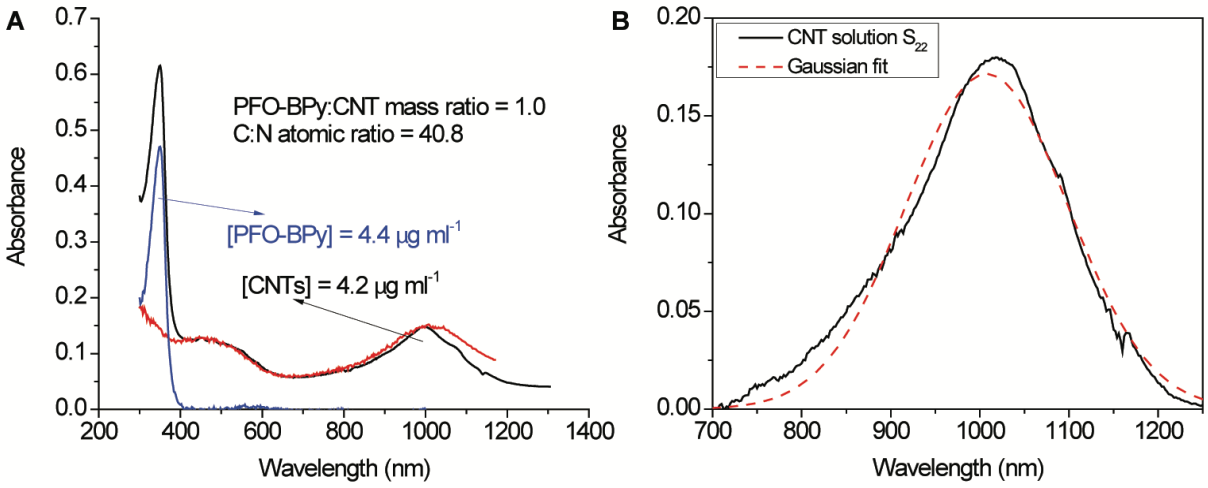

fig. S7. Optical absorbance spectra used to verify XPS atomic concentrations and CNT diameter distribution. (**A**) Black curve is an optical absorbance spectrum of an arc discharge@PFO-BPy solution in chloroform measured in a 1 cm path length cuvette showing the polymer peak centered at 350 nm and the CNT S_{33} and S_{22}. Red curve is a drop-cast arc discharge@PFO-BPy film subject to 900 ° C annealing in carbon dioxide atmosphere to completely degrade polymer. Blue spectrum is the black minus the red curve. (**B**) Gaussian fit of the CNT S_{22} to obtain a diameter distribution of 1.5 ± 0.2 nm.

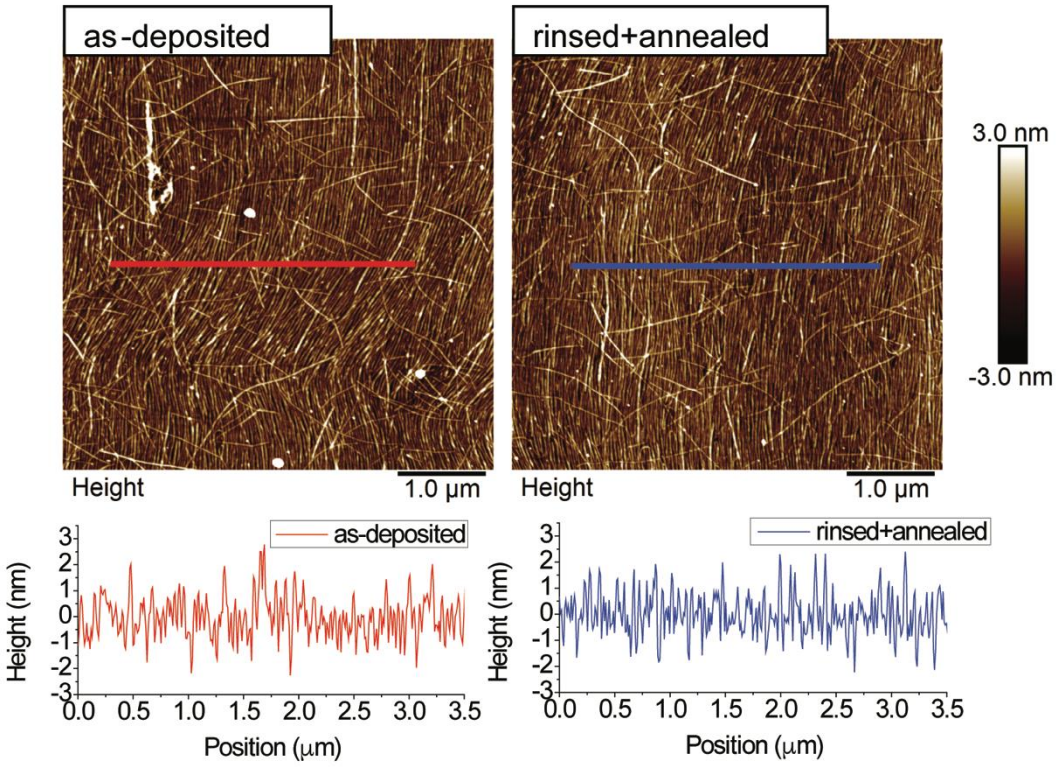

fig. S8. Atomic force microscopy height measurement used to quantify packing density for XPS calibration. AFM height maps of "as-deposited" and "rinsed+annealed" films demonstrates similar film morphology before and after treatments with average film height of ~3 nm.

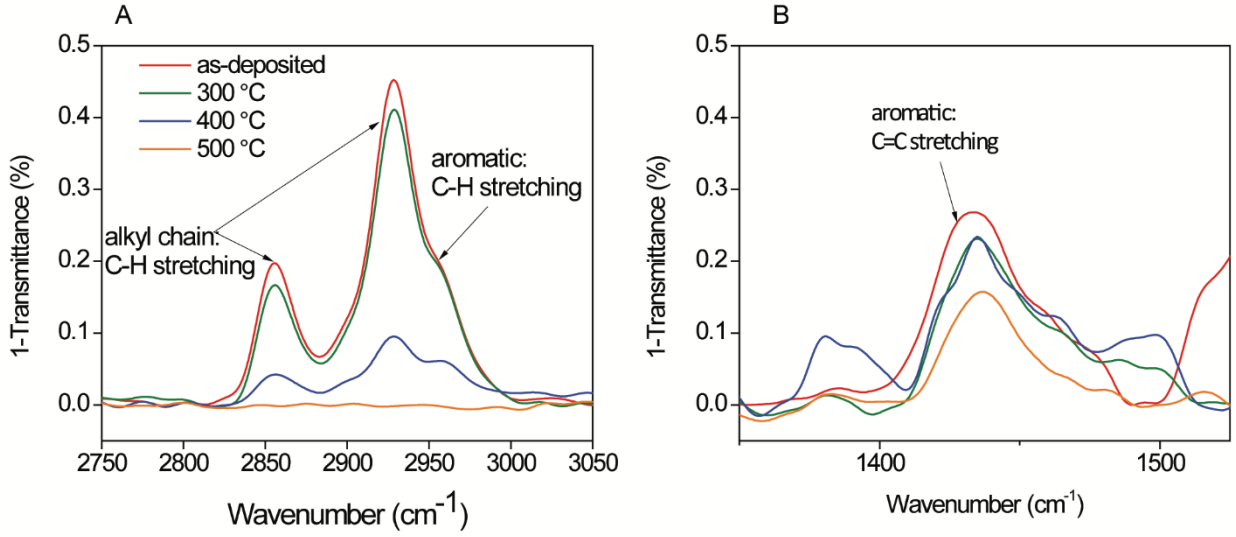

fig. S9. Temperature-dependent FTIR measurement of PFO-BPy side chains and backbone. (A) Temperature dependent FTIR measurement of the alkyl side chain C-H bonds from PFO-BPy. (B) FTIR spectra

of C=C breathing mode at 1450 cm^{-1} for PFO-BPy films indicate the presence of aromatic carbon before and after the films are annealed and that the C=C bonds from carbon in the PFO-BPy backbone begin to degrade at 500°C annealing treatment.

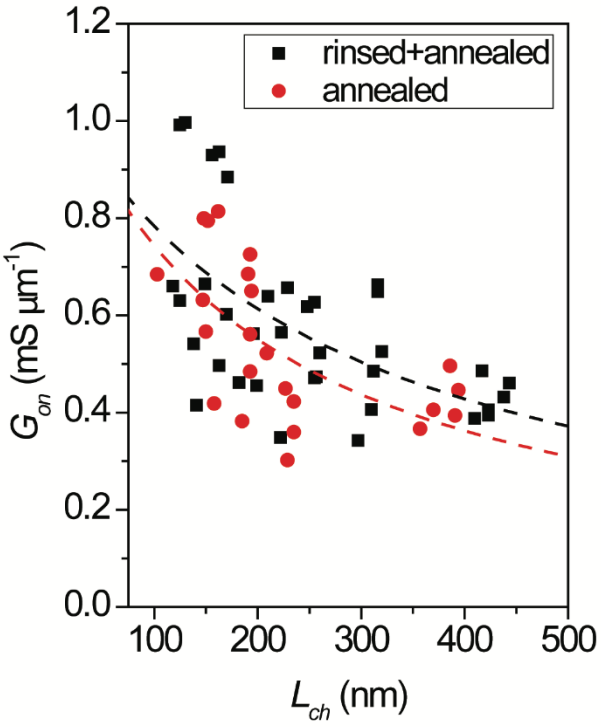

fig. S10. On-conductance comparison of "annealed" versus "rinsed + annealed" treatments. On-conductance is extracted from transfer characteristics at V_{DS} = -100 mV and V_{GS} = -10 V as a function of L_{ch} for "annealed" and "rinsed + annealed" surface treatments. Lead resistance is not subtracted from these data.

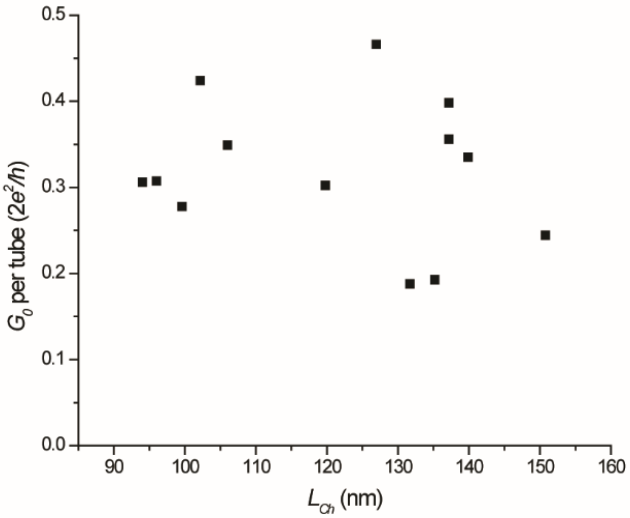

fig. S11. Conductance per tube measured for FETs with L_{ch} < 150 nm. On-state conductance is normalized to the number of CNTs spanning *S*-*D* electrodes for 13 devices.

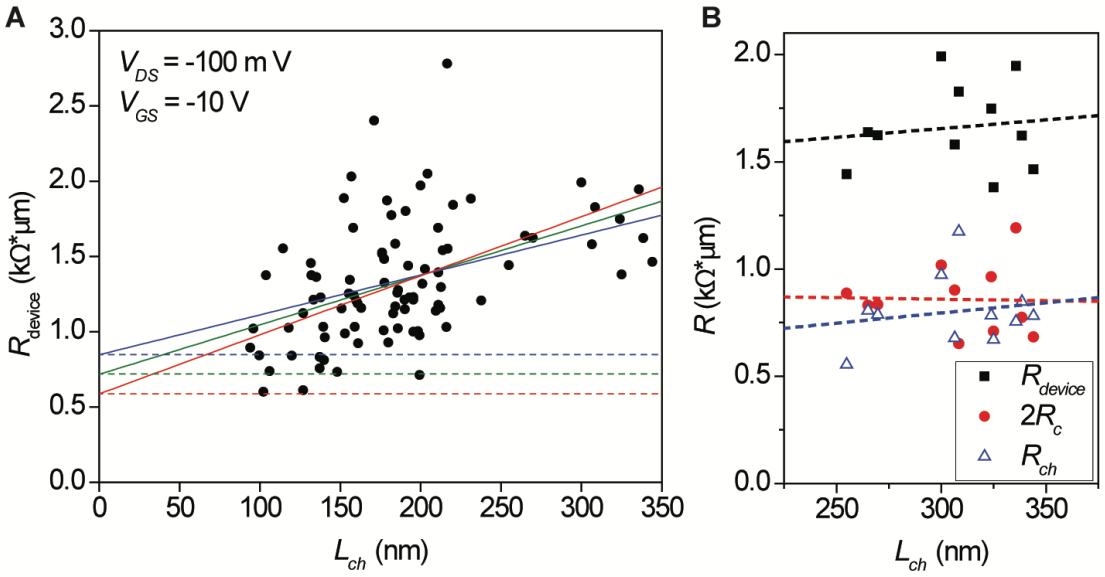

fig. S12. Contact resistance and mean free path extraction. (**A**) Transmission line analysis of R_{device} vs. L_{ch} using equation (1) of the main text to extract $2R_c$ and L_{MFP}. Red lines correspond to a lower bound for $2R_c$ and L_{MFP}, green lines are the original fit, and blues lines correspond to the upper bound. (**B**) YFM extracted $2R_c$ and channel resistance (R_{ch}) for 11 separate devices as a function of channel length. Linear fits demonstrate that R_{ch} decreases with L_{ch} while $2R_c$ is constant.

table S1. Surface treatment XPS summary. *Non-negligible concentrations of carbon (4.0×10^{14} atoms cm^{-2}) and nitrogen (5.6×10^{12} atoms cm^{-2}) measured on blank substrates are accounted for and subtracted from the CNT array values for each element, respectively. Reduction percentages are reported in parentheses for "rinsed", "annealed", and "rinsed+annealed" treatments.

	Total C* (10^{15} atoms cm^{-2})	**C from PFO-BPy inferred from N density (10^{15} atoms cm^{-2})**	**Total N* (10^{13} atoms cm^{-2})**	**Total Cl (10^{13} atoms cm^{-2})**
		C from sources other than PFO-BPy (10^{15} atoms cm^{-2})		
As-deposited	2.68 ± 0.12	1.25 ± 0.06	6.41 ± 0.28	1.67 ± 0.46
		1.43 ± 0.10		
Rinsed	2.45 ± 0.16 (*RR* = 8.5 ± 2.5%)	1.14 ± 0.03 (*RR* = 8.9 ± 3.2%)	5.83 ± 0.18 (*RR* = 8.9 ± 3.2%)	0.77 ± 0.02 (*RR* = 53.8 ± 5.2%)
		1.31 ± 0.12 (*RR* = 8.0 ± 2.3%)		
Annealed	1.83 ± 0.18 (*RR* = 31.8 ± 5.4%)	0.61 ± 0.36 (*RR* = 50.7 ± 0.9%)	5.57 ± 0.33 (*RR* = 12.6 ± 1.7%)	~0 (*RR* = ~100%)
		1.22 ± 0.14 (*RR* = 15.1 ± 10.0%)		
Rinsed + Annealed	1.62 ± 0.05 (*RR* = 33.7 ± 2.5%)	0.53 ± 0.01 (*RR* = 57.8 ± 1.4%)	4.8 ± 0.09 (*RR* = 25.1 ± 2.53%)	~0 (*RR* = ~100%)
		1.1 ± 0.04 (*RR* = 23.1 ± 2.9%)		

table S2. CNT FET performance comparisons. Key metrics for CNT array FETs produced in this work compared to previous state-of-the-art and simulated/extrapolated CNT FETs (*1, 17, 19, 74*).

	Reference	Material / channel length (nm)	On-state conductance ($\mu S\ \mu m^{-1}$) per CNT	Highest I_{on} ($\mu A\ \mu m^{-1}$)	I_{on}/I_{off}	Density (CNTs μm^{-1})
Experimental	**This work**	**Solution CNT array/ 100**	**1700** **0.47 G_o**	**900**	**10^3 - 10^7**	**50**
	Shulaker, Stanford, *IEEE IEDM* 2014 [19]	CVD CNT array / 400	120 0.015 G_0	120	10^4 - 10^5	100
	Cao, IBM, *Nature Nanotech.* 2013 [17]	Solution CNT array / 120	250 0.003 G_0	130	10 - 10^3	1000
Hypothetical	Ouyang, Univ. of Florida, *Solid State Electron.* 2011 [74]	Simulated CNT array / 100	1200 0.15 G_0	720	10^4	50
	Franklin, IBM, *Nano Lett.* 2012 [1]	Hypothetical, extrapolated from single CNT FET data / 10	1300 0.04 G_0	630	10^3	200